Graphene nanoribbons are internalized by human primary immune cell subpopulations maintaining a safety profile: A high-dimensional pilot study by single-cell mass cytometry

Claudia Fuoco, Xiangfeng Luan, Laura Fusco, Federica Riccio, Giulio Giuliani, Hazel Lin, Marco Orecchioni, Cristina Martín, Gianni Cesareni, Xinliang Feng, et al.

Graphene nanoribbons are internalized by human primary immune cell subpopulations maintaining a safety profile: a high-dimensional pilot study by single-cell mass cytometry

Claudia Fuoco,[1,#] Xiangfeng Luan,[2,3,#] Laura Fusco,[4,#] Federica Riccio,[1,#] Giulio Giuliani,[1] Hazel Lin,[3,] Marco Orecchioni,[5] Cristina Martín,[3] Gianni Cesareni,[1] Xinliang Feng,[6] Yiyong Mai,[2,] Alberto Bianco,[3,*] Lucia Gemma Delogu[4,*]*

[1]Department of Biology, University of Rome Tor Vergata, Rome, Italy

[2]School of Chemistry and Chemical Engineering, Frontiers Science Center for Transformative Molecules, Shanghai Key Laboratory of Electrical Insulation and Thermal Ageing, Shanghai Jiao Tong University, 800 Dongchuan Road, Shanghai 200240, P. R. China.

E-mail: mai@sjtu.edu.cn

[3]CNRS, Immunology, Immunopathology and Therapeutic Chemistry, UPR 3572, University of Strasbourg, ISIS, 67000 Strasbourg, France.

E-mail: a.bianco@ibmc-cnrs.unistra.fr

[4]Department of Biomedical Sciences, University of Padua, 35121 Padua, Italy. E-mail: luciagemma.delogu@unipd.it

[5]La Jolla Institute for Immunology, La Jolla, CA, USA

[6]Center for Advancing Electronics Dresden, Faculty of Chemistry and Food Chemistry, Technische Universität Dresden, Mommsenstrasse 4, 01062, Dresden, Germany

# These authors equally contributed to the work

Keywords: two-dimensional materials, biocompatibility, immune system, nanomedicine, CyTOF

Abstract

Graphene nanoribbons (GNRs) are emerging graphene materials showing clear promising applications in the biomedical field. The evaluation of GNR biocompatibility at the immune level is a critical aspect of their clinical translation. Here, we report the *ex vivo* immune profiling and tracking of GNRs at the single-cell level on eight human blood immune cell subpopulations. We selected ultra-small (GNRs-I-US) and small GNRs (GNRs-I-S), with an average length of 7.5 and 60 nm, respectively. GNRs were functionalized with ^{115}In to trace their cell interactions by single-cell mass cytometry. Both materials are highly biocompatible and internalized by immune cells without inducing significant functional changes. GNRs-I-US interacted to a greater extent with myeloid dendritic cells (mDCs) and classical monocytes, while GNRs-I-S mainly interacted with mDCs. These results demonstrate that structurally precise GNRs are efficiently internalized by immune cells. In addition, our chemical and methodological single-cell approach can be applied to other cell types using various carbon-based nanomaterials, bringing new insights into their safety and future biomedical applications.

1. Introduction

GNRs are finite-sized graphene materials with narrow widths showing a lot of promise in the biomedical field.[1-5] In particular, the possibility of chemical functionalization with drugs and imaging agents extends the use of GNRs to new therapeutic and diagnostic strategies, including targeted chemotherapy and cell imaging. [6-9] We recently proved that GNRs can be efficiently degraded under oxidative conditions, providing even more biomedical opportunities. [10] In this context, assessing the immune compatibility of nanomaterials and their cellular tracking is critical for any clinical translation. [11,12] The possible systemic administration of GNRs as future nanomedicines will result in their interaction with the immune cells present in the bloodstream. Therefore, revealing the impact of GNRs and their interactions with the complexity of immune cell responses is a key aspect of translational biomedicine.

Effective research on safety should provide new insights into a comprehensive picture of nanomaterial biological interactions at the single-cell level. Single-cell mass cytometry (CyTOF) has shown an unprecedented ability to phenotypically and functionally profile complex cellular systems, particularly those related to the immune system. [13-15] CyTOF strategy is based on elemental mass spectrometry to detect metal element-tagged probes (e.g., labeled antibodies), allowing parameter discrimination based on their mass/charge ratio, with no overlap or undesired signal background. [16] However, carbon-based materials cannot be directly detected by mass cytometry. To overcome this drawback, we recently reported the conjugation of graphene oxide with $AgInS_2$ nanocrystals enabling its detection by CyTOF. [17]

Going far beyond state of the art, we developed in this work a new straightforward method of functionalization enabling the cellular tracking of GNRs by the high dimensional approach of single-cell mass cytometry. The combination of GNRs with indium was specifically chosen to make GNRs visible by CyTOF through the detection in the indium channel (^{115}In) of the mass spectrometer, while guaranteeing the inertness of indium on cell viability and functionality. In addition, indium was selected because of its compatibility with the major commercial metal-tagged antibodies, without overlapping with the currently available CyTOF panels, which include more than 30 metal-tagged antibodies used for the immune-phenotyping and the analysis of the immune cell functionality.

2. Results and discussion

2.1 Material characterization and study design

In contrast to other carbon nanomaterials, such as graphene or graphene oxide, GNRs, obtained by bottom-up organic synthesis, are endowed with a controlled structure at the atomic level, ensuring higher reproducibility of the synthesis. This characteristic makes them of great interest

in nanomedicine, where reproducibility is among the keys to sustainable use. For this study, we selected two types of GNRs defined as ultra-small (GNRs-I-US) and small GNRs (GNRs-I-S). The starting GNR-COOH were characterized by an average length of 7.5 and 60 nm, respectively, and a width of 1.7 nm.[18]

Using the complex pool of human peripheral blood mononuclear cells (PBMCs) as an *ex vivo* model, our functional-tracking approach permitted us to reveal the diversity of the interactions and the immune impact of GNRs-I-US and GNRs-I-S at the single-cell level across eight different immune cell types (Figure 1).

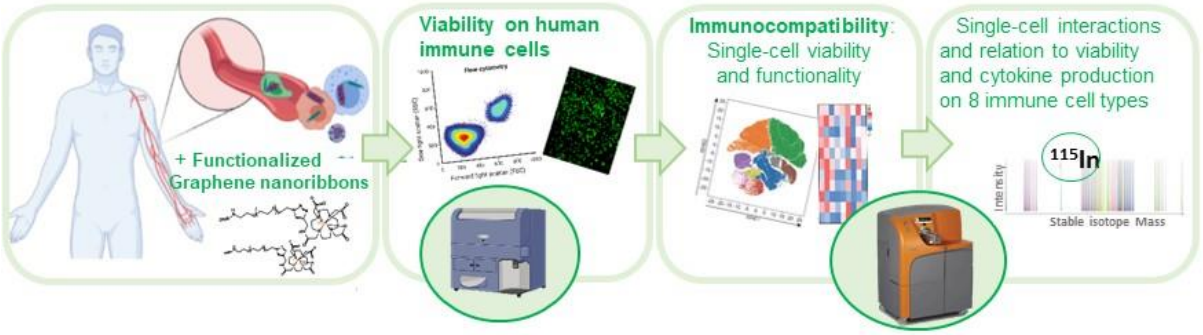

Figure 1. Schematic representation of the study workflow. PBMCs were isolated from blood samples and treated with GNRs-I-US or GNRs-I-S. Cell viability was evaluated by flow cytometry and single-cell mass cytometry. Single-cell analysis of cytokine production was performed. Brefeldin A was added the last 6 hours to prevent secretion of cytokines. Samples were stained with a panel of antibodies and analyzed by single-cell mass cytometry in a single-run experiment. The multidimensional dataset was analyzed by the FlowSOM and t-SNE algorithms.

To improve the biocompatibility of the material, long polyethylene glycol (PEG) chains with terminal amino and azide groups were covalently linked to the edges of GNR-COOH (Figure 2). The grafting of PEG greatly reduced the π-π stacking of GNRs and imparted good dispersibility in the aqueous phase. Following a copper-catalyzed click reaction, the azide groups were further functionalized by an alkyne-modified 10-[2-oxo-2-(2-propyn-1-ylamino)ethyl]-1,4,7-tris(1,1-dimethylethyl) ester (DOTA-OtBu). The final removal of the *tert*-butyl protecting groups afforded GNR-PEG-DOTA-COOH decorated with a chelating moiety able to complex different types of metal for tracking purposes. After adding indium chloride in ammonium acetate buffer (pH 5.5), we obtained the two In-labelled GNRs-I-US and GNRs-I-S.

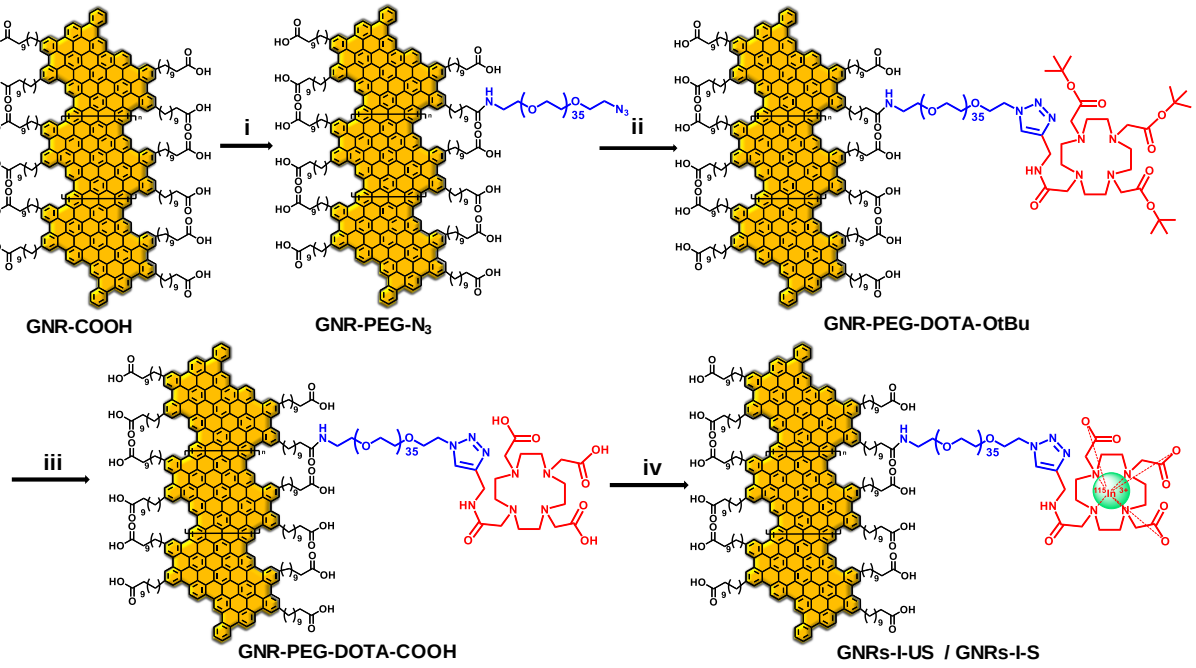

Figure 2. Synthetic route to prepare GNRs-I-US and GNRs-I-S. (i) $NH_2(CH_2CH_2O)_{35}CH_2CH_2N_3$, HOBt, EDC·HCl in THF/DMF; (ii) DOTA-O*t*Bu, sodium ascorbate, $CuSO_4{\cdot}5H_2O$ in DMF/THF/H_2O; (iii) TFA in DCM; (iv) $InCl_3$, ammonium acetate buffer at pH 5.5. The reaction has been shown in one functional group only for clarity.

The physicochemical characterization of the precursor and final GNRs was performed using Fourier-transform infrared (FT-IR) spectroscopy, thermogravimetric analysis (TGA) and X-ray photoelectron spectroscopy (XPS). From the FT-IR spectra (Figure S1), we can observe that the C=O peak of GNR-COOH at 1702 cm^{-1} shifted after the modification by PEG chains. Two new peaks appeared in the spectra of GNR-PEG-N_3. One peak attributed to the amide carbonyl stretching (corresponding to amide I vibration) is visible at about 1650 cm^{-1}, while the other related to the CN stretching and CHN deformation (corresponding to amide II vibration) is located at 1540 cm^{-1}. This result indicates that PEG has been successfully covalently grafted onto GNR-COOH. [19] Upon the click reaction between GNR-PEG-N_3 and DOTA-O*t*Bu, the azide group stretching at 2100 cm^{-1} on GNR-PEG-N_3 disappeared, [20] while C=O stretching vibration at 1733 cm^{-1} indicates the presence of the *tert*-butyl ester groups. After the hydrolysis of the *tert*-butyl ester groups, C=O stretching of the esters significantly weakened, and C=O stretching of the carboxylic groups appeared at 1685 cm^{-1}. In the case of the final products GNRs-I-US and GNRs-I-S, the vibrational frequency of the carboxylic acids of DOTA underwent a significant red shift due to the coordination with In^{3+} ions, resulting in a wide band located at around 1630 cm^{-1}.[21]

To further confirm the covalent functionalization of GNR-COOH, we analyzed the different GNR-COOH derivatives by TGA (Figure S2) under nitrogen atmosphere. Compared to the GNR-COOH profile, the weight percentage loss of the remaining GNR backbone was higher for GNR-PEG-N_3 due to the grafting of a flexible polyoxyethylene chains. As calculated according to the equation reported in the Supporting Information, the percentages of the grafted molecules on 7.5 and 60 nm GNR-PEG-N_3 are 19% and 8%, respectively. In the temperature range below 350 °C, the TGA curves of GNR-PEG-DOTA-O*t*Bu were similar to that of pure DOTA-O*t*Bu, especially between ~220 °C and ~290 °C, where the slope of the loss arises from the attached DOTA moiety.

Then, we analyzed GNRs-I-US and GNRs-I-S by XPS. The high-resolution spectra show a clear signal of In $3d_{5/2}$ and $3d_{3/2}$ peaks at 444.5 and 452.1 eV, respectively (Figure S3). The survey spectra allowed to calculate a content of indium of 0.28 at% and 0.13 at% for GNRs-I-US and GNRs-I-S, respectively, confirming the incorporation of In^{3+} into the final products.

Finally, to assess the aggregation state of the two GNRs in water, we used dynamic light scattering (DLS). GNRs-I-US and GNRs-I-S displayed a hydrodynamic diameter of 303 and 505 nm, respectively, closed to values previously reported.[18]

2.2 Biocompatibility on human peripheral blood mononuclear cells

With the two labelled GNRs in hand, we started to assess their concentration-dependent effects on cell viability by flow cytometry analysis. PBMCs were treated with different concentrations (25, 50, and 100 μg/mL) of GNRs-I-US or GNRs-I-S for 24 h, or left untreated. The selection of the concentrations was based on previous studies reported on other 2D materials with similar cell models.[22] For this experiment, we decided to use calcein staining, a cell-permeant esterase substrate that serves as a viability probe measuring both intracellular enzymatic activity and cell membrane integrity. As shown in Figure S4A-C, GNRs-I-US was highly biocompatible at each concentration tested, while GNRs-I-S induced a reduction of cell viability only at the highest concentration (100 μg/mL), suggesting superior immune compatibility conferred by the material with the smaller length.

Based on these results, we selected the intermediate concentration of 50 μg/mL to perform a simultaneous fluorescence staining of viable and dead cells by calcein and propidium iodide (PI) solutions, respectively. No significant reduction of cell viability was observed, confirming the high biocompatibility of the materials on PBMCs (Figure S4D). Our results are in line with previous studies demonstrating that similar concentrations of GNRs displayed no toxicity in other cell lines, such as osteoblasts[23] and human epithelium cells.[24]

2.3 Tracking and analysis of GNRs-I-US and GNRs-I-S at CyTOF

Subsequently, to evaluate the specific impact of the different length GNRs on cell viability and interactions with the distinct immune cell subpopulations, PBMCs were treated with 50 μg/mL of GNRs-I-US or GNRs-I-S for 24 h or left untreated and analyzed by CyTOF.

The viSNE computational approach was applied to obtain a single-cell resolution plot with eight types of CD45+ immune cell populations (Figure 3A). In detail, we identified lymphocytes (T CD8, T CD4, and B), natural killer (NK) cells, myeloid dendritic cells (mDCs), classical monocytes, nonclassical monocytes, and plasmacytoid dendritic cells (pDCs). As shown in Figure S5, analyses were performed measuring the expression of 11 cell surface activation markers (e.g., CD38, CD27, HLA-DR, CD123, CD45RA, CD16, CD3, CD8, CD19, CD14, and CD11c).

GNRs-I-US and GNRs-I-S cell interactions evaluated by indium mean intensity in PBMC populations at the single-cell level are reported as heat maps and histograms (Figure 3B-C). GNRs-I-US interacted to a greater extent with the different immune cell types analyzed, and in particular with mDCs and classical monocytes, while GNRs-I-S mainly interacted with mDCs. Rhodium, a live-cell membrane-impermeable atom, was then used to discriminate dead cells from live cells. Interestingly, the different material interactions among and within the treated cell subpopulations did not trigger a loss of cell viability. Indeed, in Figure 3D, displaying histograms related to Rh mean intensity in PBMC subpopulations, no significant effects induced by the materials on immune cell viability were observed.

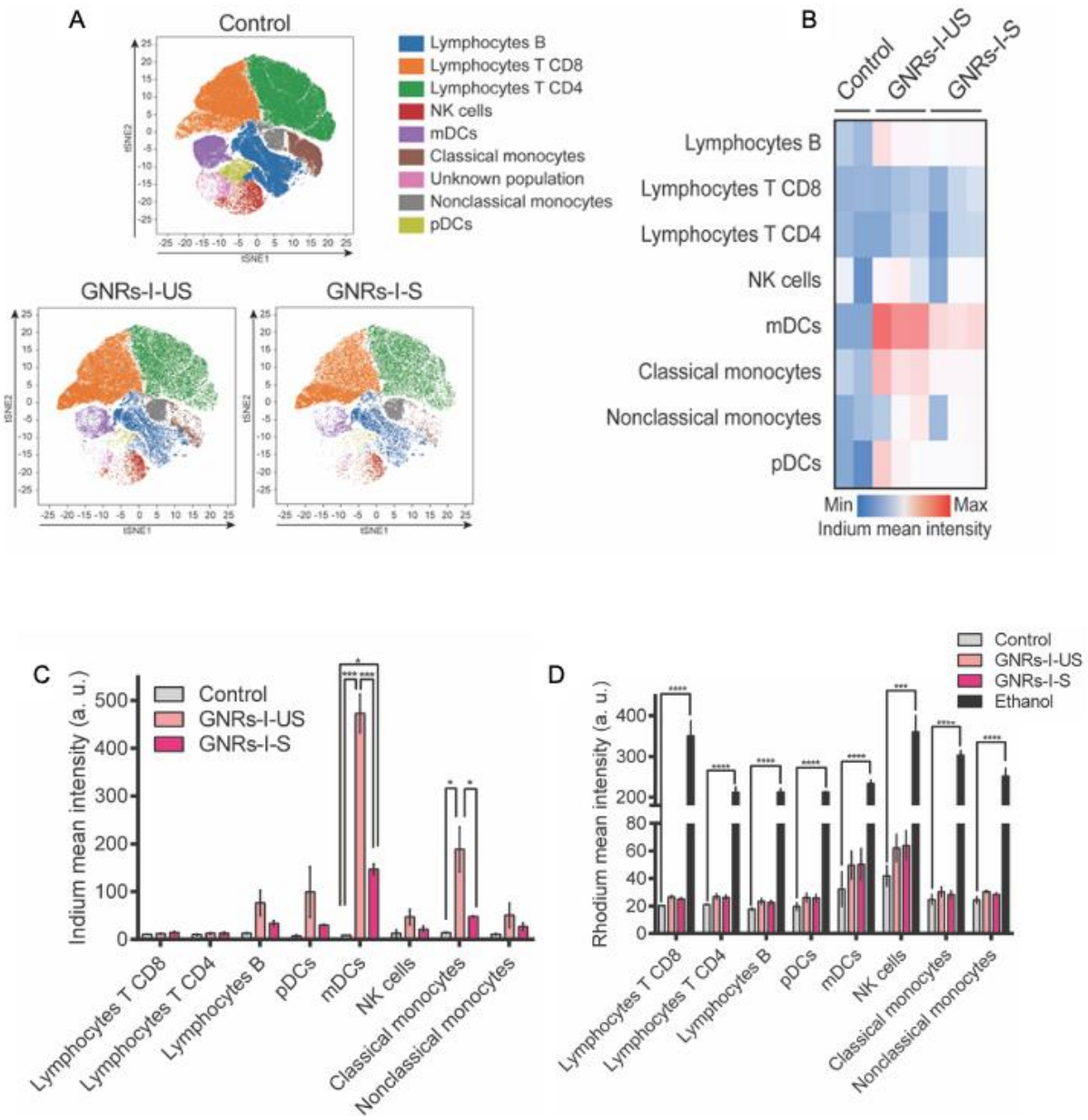

Figure 3. Tracking and analysis of GNRs-I-US and GNRs-I-S on human PBMCs. PBMCs were treated GNRs-I-US or GNRs-I-S (50 µg/mL) for 24 h and analysed by mass cytometry. **A)** Blood cell populations were identified using the FlowSOM clustering algorithm and mapped onto viSNE maps to facilitate result interpretation (NK cells = natural killer cells, mDCs = myeloid dendritic cells, pDCs = plasmacytoid dendritic cells). **B)** Heatmap showing the expression profile of the identified cell populations. **C)** Bar plot showing the indium mean intensity in cell populations for each condition reported as arbitrary units (a. u.). **D)** Bar plot illustrating rhodium mean intensity in cell populations for each condition reported as arbitrary units (a. u.). Data are reported as mean ± S.E.M., Control n = 2, GNRs-I-US n = 3, GNRs-I-S n = 3, Ethanol n = 3. Statistical significance was evaluated by a One-way ANOVA for each cell population. * $p < 0.05$, *** $p < 0.001$, **** $p < 0.0001$.

Moreover, we proved the high biocompatibility of the materials on all immune cell subpopulations studied, regardless of the interaction level (Figure 4 and Figure S6A). Indeed, for GNR-I-US the presence of the materials on mDCs was not related to a decrease in viability. The biocompatibility of the materials was corroborated by an additional viability assay, as reported in the bar plot showing platinum mean expression in blood cell populations (Figure S5E).

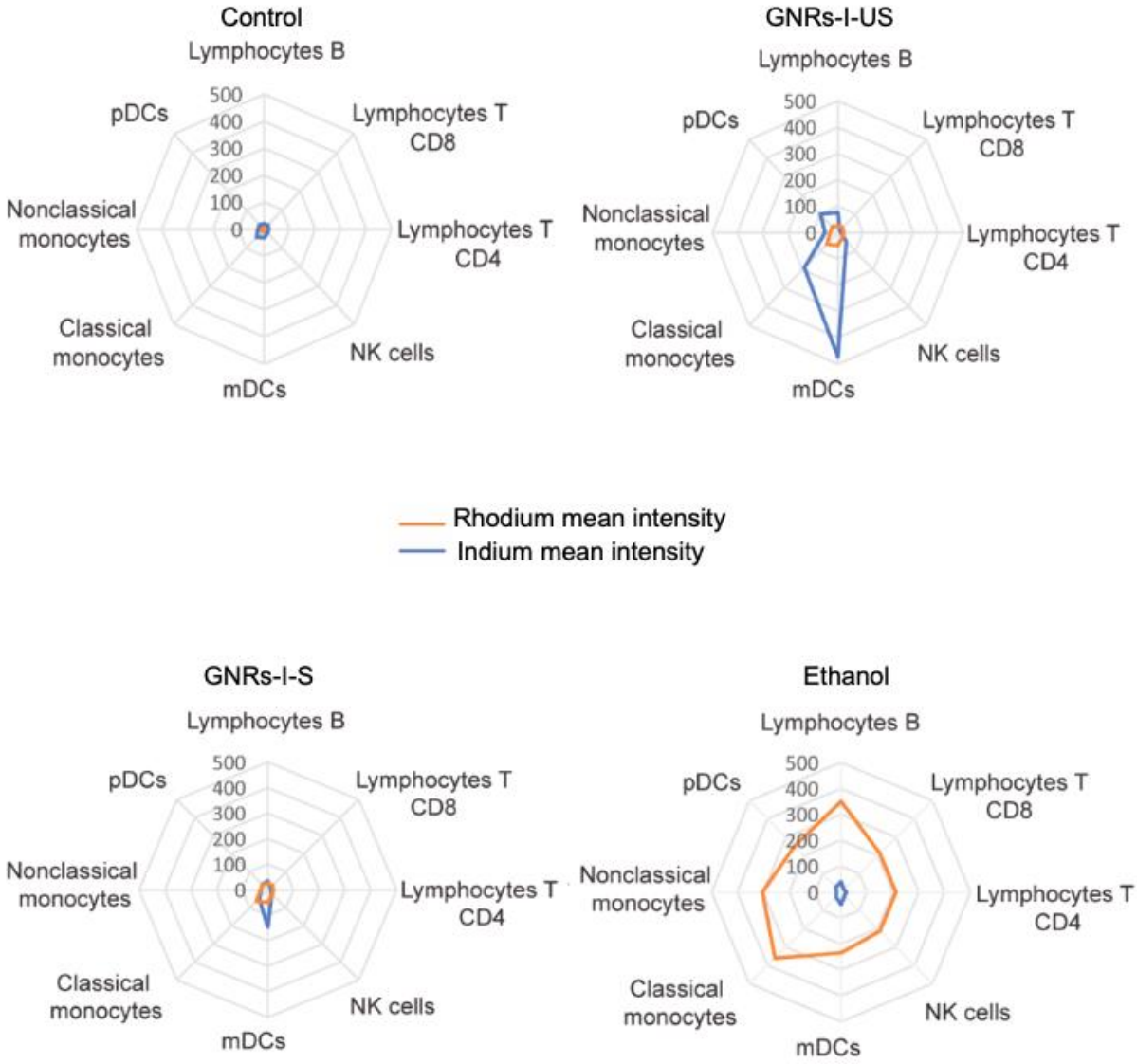

Figure 4. Biocompatibility analysis of GNRs-I-US and GNRs-I-S on human PBMCs. Radar plots representing the impact on viability (orange) vs the material tracking (blue), expressed as rhodium and indium median intensity, respectively, in all immune cell types. Data are reported as mean ± S.E.M., Control n = 2, GNRs-I-US n = 3, GNRs-I-S n = 3, Ethanol n = 3. Statistical significance was evaluated by a One-way ANOVA for each cell population. * $p < 0.05$, *** $p < 0.001$, **** $p < 0.0001$.

2.4 Immune cell functionality at CyTOF

Based on our experience with the pandemic, we have learned that functional perturbations of immune cells are involved in several aspects of human health. [25] Therefore, after exposure of PBMCs to 50 μg/mL of GNRs-I-US or GNRs-I-S for 24 h, we assessed the immune cell functionality through the measurement of several intracellular cytokines, including interleukin (IL)-5, IL-4, monocyte chemoattractant protein-1 (MP1)-b, tumor necrosis factor (TNF)-α, IL-6, IL-2, IL-17A, IL17F, interferon (IFN)-g, granzyme B and perforin, by CyTOF (Figure 5). Before the last 6 h of the test, brefeldin A was added to the medium to block cytokine secretion. Heat maps represent the median expression values of the cytokines analyzed in all immune cell subpopulations identified after treatment with of GNRs-I-US or GNRs-I-S (Figure 5A).

Considering that classical monocytes and mDCs were the main subpopulations able to interact with the materials, as revealed by the indium detection, data are also shown as histograms for these subsets (Figure 5B-C). Overall, GNRs-I-US caused a slight but non-significant increase of all cytokines in classical monocytes, while only IL-6 augmented in mDCs. On the other hand, GNRs-I-S elicited a slight but non-significant increase of IL-5 and IL-4 in mDCs. Furthermore, the materials were able to induce a general downregulation of perforin and granzyme B in mDCs, proteins that together mediate the apoptosis of target cells after exposure to pro-inflammatory stimuli in many cell subsets. [26,27]

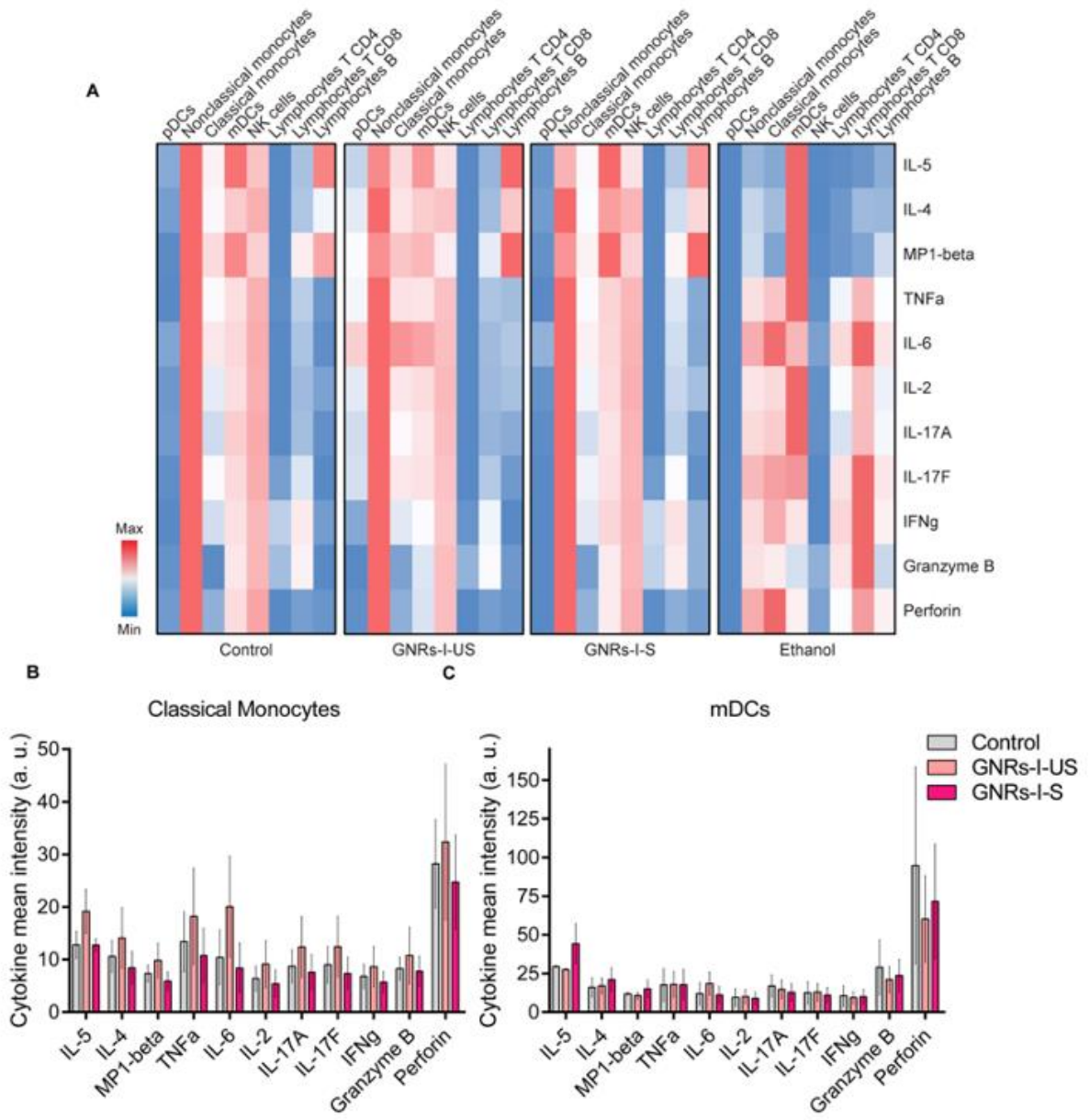

Figure 5. Production of cytokines in PBMCs. **A)** Heat maps showing the production of cytokines after exposure of PBMCs to GNRs-I-US or GNRs-I-S (50 µg/mL) for 24 h and corresponding histograms showing the mean intensity for each cytokine focusing on **B)** classical monocytes and **C)** mDCs, the main immune subpopulations interacting with the materials. Data are reported as mean ± S.E.M. in the barplots, Control n = 2, GNRs-I-US n = 3, GNRs-I-S n = 3. Statistical significance was evaluated by a One-way ANOVA for each cytokine.

The effects of the GNR materials on cytokine production, although non-significant, were consistent with their interactions with these subpopulations. However, the absence of significant changes in cytokine levels, confirms their high immune compatibility, regardless of the interaction extent, as shown for TNFα, a cytokine representative of innate immunity (Figure 6 and Figure S6B). Even considering all the other cytokines, no significant correlations between cytokine production and the cell interaction extent were observed for GNRs-I-US (Figure S7) and GNRs-I-S (Figure S8).

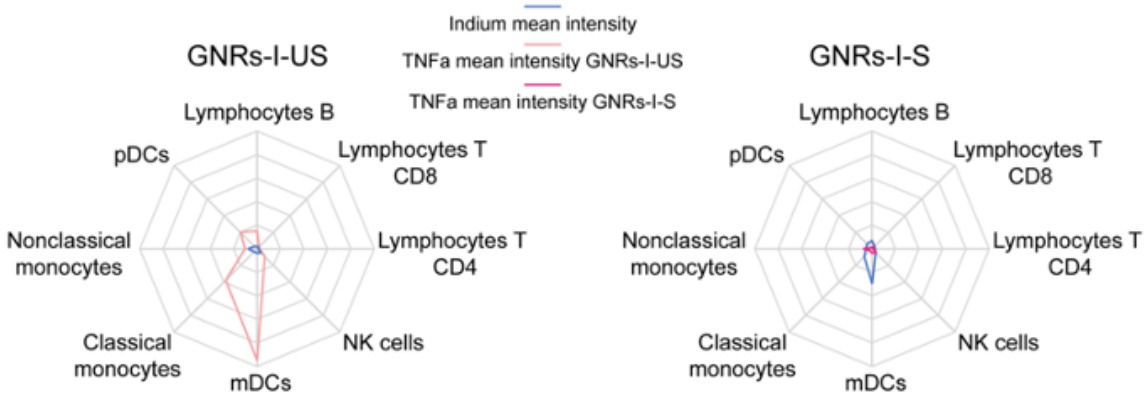

Figure 6. Production of TNFα in PBMCs. Radar plots represent the impact on production (light and dark pink for GNRs-I-US and GNRs-I-S, respectively), expressed as TNFα mean intensity, vs the material tracking (blue), expressed as indium mean intensity, for all immune cell types after exposure of PBMCs to GNRs-I-US or GNRs-I-S (50 µg/mL) for 24 h. Control n = 2, GNRs-I-US n = 3, GNRs-I-S n = 3. Statistical significance was evaluated by a One-way ANOVA for each cytokine.

The effects of the materials on the secretion of IL-6 and TNFα in PBMC supernatants were also evaluated by ELISA analysis (Figure S9), indeed their secretion occurred in the first hours of incubation time. Therefore, after exposure of PBMCs to GNRs-I-US or GNRs-I-S for 24 h, both materials elicited the production of IL-6, while only GNRs-I-S was able to induce a higher release of TNFα. The difference in IL-6 and TNFα levels observed by ELISA compared to CyTOF analysis is due to the different methodology of the two techniques, suggesting an early secretion of these cytokines induced by GNRs. Finally, we have studied the uptake of both GNRs into PBMCs using transmission electron microscopy (TEM) imaging. PBMCs were incubated with GNRs-I-US or GNRs-I-S at 50 µg/mL for 24 h. Monocytes and lymphocytes

are the main cell types that are found in PBMCs. We observed that the material was only inside monocytes (see representative images in Figure S10), in good correlation with the data obtained by CyTOF.

3. Conclusions

The results obtained in this study in terms of viability and functionality are of great interest, particularly in view of extensive literature by us and others showed for several types of carbon-based materials, in particular graphene, where the overall safety and possible inflammatory action are still under debate. [28-33]

In summary, studying nanomaterials and their interactions with the immune system is a prerequisite for understanding their safety profile. A system-wide strategy was translated here to graphene nanoribbons to cover the knowledge gap on their interaction with immune cells.[34,35] GNRs with two specific, well-defined structures were functionalized with indium for a thorough understanding of their immunocompatibility and their specific single-cell detection by CyTOF. We demonstrated that, independently of their size, GNRs are highly immune compatible with eight different primary human immune cell types. Our approach offers new chemical strategies of detection for future studies of GNRs in the context of biomedicine and drug delivery. In addition, we provide a reliable process for tracking GNRs that can be translated to other carbon and 2D nanomaterials to shed light on understanding their toxicological impact.

4. Material and methods

4.1 Preparation of GNR-PEG-N_3

GNR-COOH with a length of 7.5 or 60 nm (12 mg) were dispersed in tetrahydrofuran (THF) (20 mL), and the mixture was sonicated for 2 h. A N, N-Dimethylformamide (DMF 7 ml) solution containing 1-(3-dimethylaminopropyl)-3-ethylcarbodiimide hydrochloride (EDC×HCl) (7 mg) and 1-hydroxybenzotriazole (HOBt) (4.9 mg) were added to GNR-COOH and the reaction mixture was stirred for 30 min at 0°C. After adding $NH_2(CH_2CH_2O)_{35}CH_2CH_2N_3$ (47 mg), the dispersion was stirred at room temperature for 24 h and then filtered. During this period, every six hours, the flask was ultrasonicated for 1 h. The filtrate was washed with THF (50 mL), DMF (50 mL), methanol (100 mL), and H_2O (100 mL), and recovered as a black powder.

4.2 Preparation of GNR-PEG-DOTA-OtBu

GNR-PEG-N_3 with a length of 7.5 or 60 nm (10 mg) and 10-[2-oxo-2-(2-propyn-1-ylamino) ethyl]-1,4,7-tris(1,1-dimethylethyl) ester (DOTA-OtBu, 20mg) were dispersed in THF (30 mL) and sonicated for 2 h. To this reaction mixture, sodium ascorbate (6.5 mg), 1 ml of aqueous $CuSO_4 \cdot 5H_2O$ (4 mg) and 15 ml of DMF were then added and stirred at 60 °C for 48 h and filtered. During this period, every eight hours, the reaction mixture was ultrasonicated for 1 h. The filtrate was washed twice with THF (50 mL), DMF (50 mL), and H_2O (100 mL), and recovered as a black powder.

4.3 Preparation of GNR-PEG-DOTA-COOH

GNR-PEG-DOTA-O*t*Bu with a length of 7.5 or 60 nm (5 mg) were dispersed in 12 mL of 1:1 dichloromethane/trifluoroacetic acid (DCM/TFA) and sonicated for 2 h. The reaction mixture was stirred at room temperature for 12 h and filtered. During this period, every four hours the flask was ultrasonicated for 1 h. The precipitate corresponding to 7.5 or 60 nm GNR-PEG-DOTA-COOH (4.5 mg of 7.5 nm and 4.8 mg of 60 nm) was washed with DCM (50 mL) and H_2O (100 mL), and recovered as a black powder.

4.4 Preparation of GNRs-I-US and GNRs-I-S

GNR-PEG-DOTA-COOH with a length of 7.5 or 60 nm (3.7 mg) were dispersed in 0.4 M ammonium acetate buffer (5 ml) at pH 5.5, to which $InCl_3$ (1.9 mg) was added. The reaction mixture was sonicated for 2 h and stirred at 70 °C for 1 h. The precipitate to GNRs-I-US (3.9 mg of 7.5 nm) and GNRs-I-S and (3.8 mg of 60 nm) were washed with H_2O (100 mL), and recovered as black powder.

4.5 Dynamic light scattering

DLS values were measured using a Malvern Panalytical Zetasizer Advance Series Lab (Malvern Instruments) at 25°C. The two materials were dispersed by tip sonication for 5 min with an amplitude of 33%, pulse ON 15s/ pulse OFF 3s in MilliQ® water (pH 7) at 0.1 mg/mL. All the tests were performed three times at 25 °C applying 120 s equilibration time.

4.6 PBMC culture and treatment

Buffy coats from informed, healthy donors were obtained from the University Hospital Tor Vergata in Rome. Informed signed consent was received from all the donors. Human peripheral blood mononuclear cells (PBMCs) were isolated from buffy coat by Ficoll-Paque PLUS (GE

Healthcare) density gradient centrifugation. PBMCs were cultured in RPMI-1640 medium added with FBS 10% and 1% of penicillin/streptomycin solution. GNRs were used in sterile conditions as previously reported.[36]

4.7 Flow cytometry cell viability analyses

The concentration-dependent effects of GNRs on cell viability were assessed by flow cytometry analysis. PBMCs (2.5×105 cells/well) from three independent human samples were seeded in 48-wells plates and treated with different concentrations (25, 50, and 100 μg/mL) of GNRs-I-US or GNRs-I-S for 24 h or left untreated. Cells were washed with 2% FBS in PBS (FACS Buffer), then stained with 50 μM of calcein-AM (Thermo-Fisher Scientific, C1430) at 4 °C for 10 min. Calcein is a cell-permeant esterase substrate that serves as a viability probe to measure enzymatic activity and cell membrane integrity. After staining, cells were washed twice with FACS buffer, resuspended in FACS buffer, and analyzed by a flow cytometer (Beckman Coulter CytoFEX) using blue (488 nm) excitation and fluorescence emission (517 nm).

4.8 Live/Dead cell staining

PBMCs (2.5×10^5 cells/well) from three independent human samples were seeded in 48-wells plates and treated with 50 μg/mL of GNRs-I-US or GNRs-I-S for 24 h, or left untreated. Double Staining Kit (Sigma-Aldrich, 04511) was used for simultaneous fluorescence staining of viable and dead cells. This kit contains calcein-AM and propidium iodide (PI) solutions, which stain viable and dead cells, respectively. The staining was performed according to the manufacturer's instructions. Fluorescence images were captured with a Nikon TE 2000 camera equipped with a CCD camera CoolSnap Myo controlled by Metamorph acquisition software.

4.9 Staining protocol for mass cytometry

PBMCs (2×10^6/well) from three independent human samples were seeded in a 24 multi-well plates and treated with 50 μg/mL of GNRs-I-US, GNRs-I-S for 24 h, 70% ethanol for 5 min as positive control or left untreated. In particular, for this cohort of samples (controls untreated) n=2 replicates have been analyzed due to barcoding number restriction kit protocols. For the detection of cytokines, Brefeldin A was added 5 h before the incubation ends. PBMCs were centrifuged at 900g for 10 min and incubated at 37°C for 15 min in growth media with Cell-ID Intercalator ^{103}Rh at final concentration of 1 μM in order to discriminate dead cells from live cells. ^{103}Rh is a live-cell membrane-impermeable dye. PBMCs were centrifuged at 900g for 10 min and washed in PBS without calcium and magnesium. Cells were fixed with 1 mL of Fix I

buffer for 10 min at room temperature (RT). The fixation reaction was quenched with Barcode Perm Buffer. Samples from different condition and replicates were barcoded by individually incubating them with a combination of palladium isotopes from the Cell-ID^{TM} 20-Plex Pd Barcoding Kit in Barcode Perm Buffer for 30 min at RT. Palladium staining was quenched using MaxPar Cell Staining Buffer and next samples were pooled into a single tube. This procedure allows to minimize the inter-sample staining variation. Cells were then stained using Maxpar Human Peripheral Blood Phenotyping and Human Intracellular Cytokine I Panel Kits following the manufacturer staining protocol for cell surface and cytoplasmic/secreted markers. After two washings in MaxPar Cell Staining Buffer, PBMCs were stained with 125 nM of Cell-ID Intercalator-Ir (191Ir and 193Ir) in MaxPar Fix and Perm Buffer. Next, cells were washed twice in MaxPar Cell Staining Buffer, MaxPar Water and resuspended at the concentration of $3x10^5$cells/mL in distilled water supplemented with 10% of EQTM Four Element Calibration Beads. Samples were filtered through a 30 μm filter and run into CyTOF2 platform. All reagents and antibodies were purchased from Fluidigm Corporation (Fluidigm, CA, USA).

4.10 Mass cytometry data analysis

Data were collected as fcs files. Channel intensity was normalized using calibration beads,[37] and files were debarcoded using the Debarcoder software (Fluidigm). Fcs files were uploaded on Cytobank for the downstream analysis (Beckman Coulter).[38] Cells were identified by the proportional incorporation of 191Ir (DNA1) and 193Ir (DNA2) and singlets were discriminated from doublets using the event length parameter. Next, CD61- CD66- cells (see gating strategy in Supporting Figure S5) were used for the downstream analysis. ViSNE maps in Figure 3A and Supporting Figure S5 were produced by the t-SNE algorithm using the following parameters on total events: 2000 iterations, perplexity 80, theta 0.5, seed 313704649. [39,40] The clustering channel were: CD11c, CD123, CD14, CD19, CD3, CD8, HLA-DR. The FlowSOM algorithm was applied to identify 20 metaclusters using the following sampling total events: 225 clusters, 10 iterations, seed 1324977929, hierarchical consensus clustering to determine metaclusters, no scale normalization.[41] tSNE1 and tSNE2 were used as clustering channels. To facilitate result interpretation, these metaclusters were mapped onto viSNE maps (see Supporting Figure 5D). Consulting viSNE maps in Supporting FigureS5B, we merged metaclusters showing similar expression profiles in order to obtain 9 final metaclusters (Figure 3A) corresponding to the PBMC main populations. The expression profile of such populations is shown in Figure S5B. Heatmaps were produced by exporting the intensity values from Cytobank to Excel and normalizing the expression of each protein between 0 and 1.

4.11 ELISA

Secretion of the cytokines IL-6 (BD Opt-EIA #555220) and TNF (BD Opt-EIA #555212) from PBMCs treated with 50 µg/mL of GNRs-I-US or GNRs-I-S for 24 h was assayed with ELISA kits according to the manufacturer's instructions. PHA (4 µg/mL) was added as a positive control. In short, polyvinyl microtiter 96-well plates (Falcon) were coated overnight at 4 °C with 50 µL/well of purified capture antibodies diluted in coating buffer (carbonate/bicarbonate buffer 0.05 M, pH 9.6). After washing with PBS containing 0.05% Tween (PBS-T), a blocking step was performed by adding 5% FBS in PBS (100 µL/well) for 1 h at room temperature. After washing thrice with PBS-T, 35 µL of culture supernatants from the treated cells were added in triplicate in the respective wells for 2 h at room temperature, along with a respective series of standards as provided in the kits. The plates were then washed five times with PBS-T. Secondary antibodies, as provided in the kit, were then added with HRP reagent and incubated for 1 h at room temperature. Then, the plates were washed five times with PBS-T, and the presence of cytokines in the tested supernatants was visualized by adding tetramethylbenzidine (TMB) in the presence of H_2O_2. The resulting absorbance was measured at 450 nm after stopping the reaction with 2 N H_2SO_4, after 15 min.

4.12 Transmission electron microscopy on cells

PBMCs were cultured in 6-well plates at a density of 2×10^6 cells per well and allowed to adhere before exposure to 50 µg/mL GNRs-I-US or GNRs-I-S for 24 h along with control untreated cells. After incubation, the cells were washed with cacodylate buffer twice and then fixed in 2.5% glutaraldehyde in cacodylate buffer at 4 °C overnight. Following overnight fixation, the cells were rinsed thrice with cacodylate buffer alone. Later, the cells were post-fixed with 0.5% osmium tetroxide for 1 h at room temperature and were washed thrice with Milli-Q® water. Cells were then dehydrated through a series of ethanol baths: 1× 25% ethanol for 10 min, 1× 50% ethanol for 15 min, 1× 70% ethanol for 15 min, 1× 95% ethanol for 15 min and 3× 100% ethanol for 15 min. Following dehydration, the cells were soaked in 1:1 ratio of 100% ethanol and Epon™ overnight at 4 °C. The next day, the cells were rinsed (1× 4 h) with Epon™. After soaking, the final inclusion of Epon™ into the cells was done by polymerizing Epon™ at 60 °C for 48 h. Afterwards, the polymerized blocks were removed and sliced into ultrathin sections using a diamond knife attached to a ultramicrotome cutter (Leica). The ultrathin sections were then collected on copper grids and stained with 1% uranyl acetate for 5 min followed with lead citrate staining for 2 min. Grids were then examined by TEM (Hitachi 7500).

4.13 Statistical analysis

Experiments were performed with primary cells (PBMCs) isolated from at least three different healthy donors (here defined human samples). Number of human samples were specified in the figure legends. Statistical analysis was performed by one-way ANOVA for comparison among more than three groups. Results were presented as mean ± standard error of the mean (SEM). Differences were considered significant when p-value is less than 0.05 (* $p \leq 0.05$, ** $p \leq 0.01$, *** $p \leq 0.001$, **** $p \leq 0.0001$). Plots and statistical analysis were produced using GraphPad Prism 7 software.

Data Availability Statement

The data that support the findings of this study are available from the authors upon request.

Acknowledgements

We also gratefully acknowledge the Centre National de la Recherche Scientifique (CNRS), the International Center for Frontier Research in Chemistry (icFRC), and financial support from European Union's Horizon 2020 research and innovation programme under the Marie Sklodowska-Curie grant agreement no. 734381 (CARBO-IMmap) and from the Agence Nationale de la Recherche (ANR) through the LabEx project Chemistry of Complex Systems (ANR-10-LABX-0026_CSC). We thank the financial support from the National Natural Science Foundation of China (21774076 and 52073173) and the Program of Shanghai Academic Research Leader (19XD1421700). The Instrumental Analysis Center at Shanghai Jiao Tong University is also appreciated. The authors wish to thanks L. Jacquemin for his help to record DLS values.

References

[1] J. Cai, P. Ruffieux, R. Jaafar, M. Bieri, T. Braun, S. Blankenburg, M. Muoth, A. P. Seitsonen, M. Saleh, X. Feng, K. Mullen, R. Fasel, Atomically precise bottom-up fabrication of graphene nanoribbons, Nature 466 (2010) 470-473.

[2] Y. Huang, F. Xu, L. Ganzer, F. Valduga de Almeida Camargo, T. Nagahara, J. Teyssandier, H. Van Gorp, K. Basse, L. Straasø, V. Nagyte, C. Casiraghi, M. R. Hansen, S. De Feyter, D. Yan, K. Müllen, X. Feng, G. Cerullo, Y. Mai, Intrinsic Properties of Single Graphene Nanoribbons in Solution: Synthetic and Spectroscopic Studies, J. Am. Chem. Soc. 140 (2018) 10416 –10420.

[3] W. Niu, J. Liu, Y. Mai, K. Müllen, X. Feng, Synthetic Engineering of Graphene Nanoribbons with Excellent Liquid-Phase Processability, Trends Chem. 1 (2019) 549-558.

[4] D. J. Rizzo, J. Jiang, D. Joshi, G. Veber, C. Bronner, R. A. Durr, P. H. Jacobse, T. Cao, A. Kalayjian, H. Rodriguez, P. Butler, T. Chen, S. G. Louie, F. R. Fischer, M. F. Crommie, Rationally Designed Topological Quantum Dots in Bottom-Up Graphene Nanoribbons, ACS Nano 15 (2021) 20633-20642.

[5] O. Groning, S. Wang, X. Yao, C. A. Pignedoli, G. Borin Barin, C. Daniels, A. Cupo, V. Meunier, X. Feng, A. Narita, K. Müllen, P. Ruffieux, R. Fasel, Engineering of robust topological quantum phases in graphene nanoribbons, Nature 560 (2018) 209-213.

[6] A. Gazzi, L. Fusco, M. Orecchioni, S. Ferrari, G. Franzoni, S. Yan, M. Rieckher, G. Peng, M. A. Lucherelli, I. A. Vacchi, N. D. Q. Chau, A. Criado, A. Istif, D. Mancino, A. Dominguez, H. Eckert, E. Vazquez, T. Da Ros, P. Nicolussi, V. Palermo, B. Schumacher, G. Cuniberti, Y. Mai, C. Clementi, M. Pasquali, X. Feng, K. Kostarelos, A. Yilmazer, D. Bedognetti, B. Fadeel, M. Prato, A. Bianco, L. G. Delogu, Graphene, other carbon nanomaterials and the immune system: toward nanoimmunity-by-design, J. Phys. Mater. *3* (2020) 034009.

[7] S. M. Chowdhury, C. Surhland, Z. Sanchez, P. Chaudhary, M. A. S. Kumar, S. Lee, L. A. Peña, M. Waring, B. Sitharaman, M. Naidu, Graphene nanoribbons as a drug delivery agent for lucanthone mediated therapy of glioblastoma multiforme, Nanomedicine: Nanotech. Biol. Med. 11 (2015) 109-118.

[8] N. Panwar, A. M. Soehartono, K. K. Chan, S. Zeng, G. Xu, J. Qu, P. Coquet, K.-T. Yong, X. Chen, Nanocarbons for Biology and Medicine: Sensing, Imaging, and Drug Delivery, Chem. Rev. 119 (2019) 9559-9656.

[9] P. Shende, N. Pathan, Graphene nanoribbons: A state-of-the-art in health care, Int. J. Pharm. 595 (2021) 120269.

[10] X. Luan, C. Martín, P. Zhang, Q. Li, I. A. Vacchi, L. G. Delogu, Y. Mai, A. Bianco, Degradation of Structurally Defined Graphene Nanoribbons by Myeloperoxidase and the Photo-Fenton Reaction, Angew. Chem. Int. Ed. 132 (2020) 18673-18679.

[11] D. A. Scheinberg, J. Grimm, D. A. Heller, E. P. Stater, M. Bradbury, M. R. McDevitt, Advances in the clinical translation of nanotechnology, Curr. Opin. Biotechnol. 46 (2017) 66-73.

[12] H. Liu, P. van Nooten, L. Deng, W. Cui, Clinical Translation of Nanomaterials, in Theranostic Bionanomaterials, Cui, W. & Zhao, X. Eds., (2019) 75-111.

[13] F. J. Hartmann, S. C. Bendall, Immune monitoring using mass cytometry and related high-dimensional imaging approaches, Nat. Rev. Rheumatol. 16 (2020) 87-99.

[14] S. Chevrier, Y. Zurbuchen, C. Cervia, S. Adamo, M. E. Raeber, N. de Souza, S. Sivapatham, A. Jacobs, E. Bachli, A. Rudiger, M. Stüssi-Helbling, L. C. Huber, D. J. Schaer, J. Nilsson, O. Boyman, B. Bodenmiller, A distinct innate immune signature marks progression from mild to severe COVID-19, Cell Rep. Med. 2 (2021)100166.

[15] B. Sahaf, A. Rahman, H. T. Maecker, S. C. Bendall, High-Parameter Immune Profiling with CyTOF, Meth. Mol. Biol. 2055 (2020) 351-368.

[16] M. H. Spitzer, G. P. Nolan, Mass Cytometry: Single Cells, Many Features, Cell 165 (2016) 780-791.

[17] M. Orecchioni, V. Bordoni, C. Fuoco, W. Hendrickx, G. Reina, C. Ménard-Moyon, H. Lin, S. Guo, R. Sainz, M. Zoccheddu, A. Yilmazer, G. Cesareni, K. Kostarelos, D. Bedognetti, A. Bianco, L. G. Delogu, Toward High-Dimensional Single-Cell Analysis of Graphene Oxide Biological Impact: Tracking on Immune Cells by Single-Cell Mass Cytometry, Small 16 (2020) 2000123.

[18] Y. Huang, Y. Mai, U. Beser, J. Teyssandier, G. Velpula, H. van Gorp, L. A. Straasø, M. R. Hansen, D. Rizzo, C. Casiraghi, R. Yang, G. Zhang, D. Wu, F. Zhang, D. Yan, S. De Feyter, K. Müllen, X. Feng, Poly(ethylene oxide) Functionalized Graphene Nanoribbons with Excellent Solution Processability, J. Am. Chem. Soc. 138 (2016) 10136-10139.

[19] S. Stankovich, R. D. Piner, S. T. Nguyen, R. S. Ruoff, Synthesis and exfoliation of isocyanate-treated graphene oxide nanoplatelets, Carbon 44 (2006) 3342-3347.

[20] E. Lieber, C. N. R. Rao, T. S. Chao, C. W. W. Hoffman, Infrared Spectra of Organic Azides, Anal. Chem. 29 (1957) 916-918.

[21] S. Liu, Z. He, W.-Y. Hsieh, P. E. Fanwick, Synthesis, characterization, and X-ray crystal structure of In(DOTA-AA) (AA = p-aminoanilide): a model for 111In-labeled DOTA-biomolecule conjugates, Inorg. Chem. 42 (2003) 8831-8837.

[22] L. Fusco, M. Orecchioni, G. Reina, V. Bordoni, C. Fuoco, C. Gurcan, S. Guo, N. Zoccheddu, F. Collino, B. Zavan, E. Treossi, A. Yilmazer, V. Palermo, A. Bianco, L. G. Delogu, Lateral dimension and amino-functionalization on the balance to assess the single-cell toxicity of graphene on fifteen immune cell types, NanoImpact 23 (2021) 100330.

[23] R. Ricci, N. Leite, C. Pacheco Soares, R. Canevari, F. Marciano, T. Webster, A. Lobo, Graphene oxide nanoribbons as nanomaterial for bone regeneration: Effects on

cytotoxicity, gene expression and bactericidal effect, Mater. Sci. Eng. C 78 (2017) 341-348.

[24] B. Zhang, Y. Wang, G. Zhai, Biomedical applications of the graphene-based materials, G. Mater. Sci. Eng. C 61 (2017) 953-964.

[25] C. Weiss, M. Carriere, L. Fusco, I. Capua, J. A. Regla-Nava, M. Pasquali, J. A. Scott, F. Vitale, M. A. Unal, C. Mattevi, B. Bedognetti, A. Merkoçi, E. Tasciotti, A. Yilmazer, Y. Gogotsi, F. Stellacci, L. G. Delogu, Toward Nanotechnology-Enabled Approaches against the COVID-19 Pandemic, ACS Nano 14 (2020) 6383-6406.

[26] A. Wensink, V. Kemp, J. Fermie, M. I. García-Laorden, T. Poll, C. Hack, N. Bovenschen, Granzyme K synergistically potentiates LPS-induced cytokine responses in human monocytes, Proc. Natl. Acad. Sci. U S A 111 (2014) 5974-5979.

[27] A. Cifuentes-Rius, A. Desai, D. Yuen, A. P. R. Johnston, N. H. Voelcker, Inducing immune tolerance with dendritic cell-targeting nanomedicines, Nat. Nanotech. 16 (2021) 37-46.

[28] V. Bordoni, G. Reina, M. Orecchioni, G. Furesi, S. Thiele, C. Gardin, B. Zavan G. Cuniberti, A. Bianco, M. Rauner, L. G. Delogu, Stimulation of bone formation by monocyte-activator functionalized graphene oxide: In vivo, Nanoscale 11 (2019) 19408-19421.

[29] M. Orecchioni, D. Bedognetti, L. Newman, C. Fuoco, F. Spada, W. Hendrickx, F. M. Marincola, F. Sgarrella, F. A. Rodrigues, C. Ménard-Moyon, G. Cesareni, K. Kostarelos, A. Bianco, L. G. Delogu, Single-cell mass cytometry and transcriptome profiling reveal the impact of graphene on human immune cells, Nat. Comm. 8 (2017) 1109.

[30] J. Russier, V. Léon, M. Orecchioni, E. Hirata, P. Virdis, C. Fozza, F. Sgarrella, M. Prato, E. Vazquez, A. Bianco, L. G. Delogu, Few-Layer Graphene Kills Selectively Tumor Cells from Myelomonocytic Leukemia Patients, Angew. Chem. Int. Ed. 56 (2017) 3014-3019.

[31] G. Peng, M. F. Montenegro, C. N. M. Ntola, S. Vranic, K. Kostarelos, C. Vogt, M. S. Toprak, T. Duan, K. Leifer, L. Bräutigam, J. O. Lundberg, B. Fadeel, Nitric oxide-dependent biodegradation of graphene oxide reduces inflammation in the gastrointestinal tract, Nanoscale 12 (2020) 16730-16737.

[32] S. Bengtson, K. B. Knudsen, Z. O. Kyjovska, T. Berthing, V. Skaug, M. Levin, I. K. Koponen, A. Shivayogimath, T. J. Booth, B. Alonso, A. Pesquera, A. Zurutuza, B. L. Thomsen, J. T. Troelsen, N. R. Jacobsen, U. Vogel, Differences in inflammation and acute phase response but similar genotoxicity in mice following pulmonary exposure to graphene oxide and reduced graphene oxide, PLoS One 12 (2017) e0178355.

[33] L. Newman, D. A. Jasim, E. Prestat, N. Lozano, I. de Lazaro Y. Nam, B. M. Assas, J. Pennock, S. J. Haigh, C. Bussy, K. Kostarelos, Splenic Capture and In Vivo Intracellular Biodegradation of Biological-Grade Graphene Oxide Sheets, ACS Nano 14 (2020) 10168-10186.

[34] N. Damond, S. Engler, V. R. T. Zanotelli, D. Schapiro, C. H. Wasserfall, I. Kusmartseva, H. S. Nick, F. Thorel, P. L. Herrera, M. A. Atkinson, B. Bodenmiller, A Map of Human Type 1 Diabetes Progression by Imaging Mass Cytometry, Cell Metab. 29 (2019) 755-768.e5.

[35] C. Giesen, H. A. Wang, H. D. Schapiro, N. Zivanovic, A. Jacobs, B. Hattendorf, P. J. Schuffler, D. Grolimund, J. M. Buhmann, S. Brandt, Z. Varga, P. J. Wild, D. Gunther, B. Bodenmiller, Highly multiplexed imaging of tumor tissues with subcellular resolution by mass cytometry, Nat Methods 11 (2014) 417-22.

[36] L.G. Delogu, S. M. Stanford, E. Santelli, A. Magrini, A. Bergamaschi, K. Motamedchaboki, N. Rosato, T. Mustelin, N. Bottini, M. Bottini, Carbon nanotube-based nanocarriers: The importance of keeping it clean, J. Nanosci. Nanotechnol. 10 (2010) 5293-5301.

[37] R. Finck, E. F. Simonds, A. Jager, S. Krishnaswamy, K. Sachs, W. Fantl, D. Pe'er, G. P. Nolan, S. C. Bendall, Normalization of mass cytometry data with bead standards, Cytometry A 83 (2013) 483-494.

[38] N. Kotecha, P. O. Krutzik, J. M. Irish, Web-based analysis and publication of flow cytometry experiments, Curr. Protoc. Cytom. 53 (2010) 10.17.1-10.17.24.

[39] L. van der Maaten, G. Hinton, Visualizing Data using t-SNE, J. Mach. Learn. Res. 9 (2008) 2579-2605.

[40] E-a. D. Amir, K. L. Davis, M. D. Tadmor, E. F. Simonds, J. H. Levine, S. C. Bendall, D. K. Shenfeld, S. Krishnaswamy, G. P. Nolan, D. Pe'er, viSNE enables visualization of high dimensional single-cell data and reveals phenotypic heterogeneity of leukemia, Nat. Biotechnol. 31 (2013) 545-552.

[41] S. Van Gassen, B. Callebaut, M. J. Van Helden, B. N. Lambrecht, P. Demeester, T. Dhaene, Y. Saeys, FlowSOM: Using self-organizing maps for visualization and interpretation of cytometry data, Cytometry A 87 **(**2015) 636-645.